Supplement of The Cryosphere, 12, 2689–2705, 2018
https://doi.org/10.5194/tc-12-2689-2018-supplement

The Cryosphere
Open Access

Supplement of

Multi-channel and multi-polarization radar measurements around the NEEM site

Jilu Li et al.

Correspondence to: Jilu Li (jiluli@ku.edu)

S1 Description of radar system

As shown in Fig. S1, the system is composed of a digital section, RF (Radio Frequency) section, and antennas. The digital system is comprised of a waveform generator and a multi-channel data acquisition system. The RF section

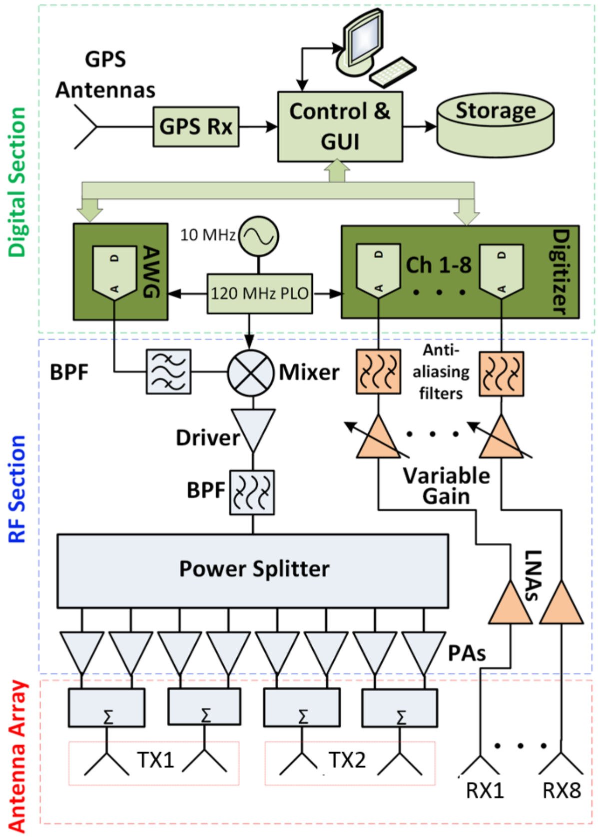

Figure S1: The simplified block diagram of the multi-channel radar system.

consists of two transmitters (denoted TX1 and TX2) and eight separate analog receiver channels with variable gain (denoted RX1 to RX8). Multiple receivers are used to provide beamforming capabilities in post processing. The digital waveform generator produces an offset video chirp from 15 to 45 MHz, which is up-converted to 135-165 MHz using a 120 MHz local oscillator mixing stage. The signal from the transmitter splits eight ways and feeds into four sets of two 50-Watt power amplifier banks (eight amplifiers for a combined peak power of 400 Watts). Each analog receiver is composed of a low-noise amplifier (LNA), a digitally controlled variable gain stage and an anti-aliasing filter with a 3-dB bandwidth of 130-170 MHz. The output signals from the analog receivers are captured by the data acquisition system using 12-bit analog-to-digital converters (ADCs) operating at a rate of 120 MSPS. Data from each of the receivers are stored in binary format with GPS-based time stamps for geo-location in post-processing.

S2 Antenna geometry, radiation patterns and installation

The radiating structure consists of an array of twelve log-periodic antennas, each with a gain of about 6.7 dB. Each antenna is composed of 17 elements (dipoles). Fig. S2 shows the geometry and the radiation pattern of one of the 17-element log-periodic antennas [Harish, 2008]. See Fig. S3 for two pictures taken during the survey showing the antenna and GPS receiver installation on a tracked vehicle. Fig. S4 shows the simulated effect of the truss on the radiation pattern of the antenna. Fig. S5 illustrates the truss construction and geometry.

S3 Receive channel equalization method and results

We used co-polarization reflections from three distinct, specular, and continuous layers at depths of 1142, 1181, and 1271 m (see Fig. S6a) to determine channel-to-channel differences. A total number of 12500 data records were used in this calibration step over a distance of about 1000 m along a straight path from the NEEM ice core site to Circle 1. Every 10 compressed pulses were stacked together and averaged (coherent integration) for better detection of these three layers; the two-way propagation time, amplitude, and phase were then extracted for each layer and channel, with 1250 samples. Channel RX2 and RX6 were selected as the reference channels for RX1~RX4 (H-polarization) and RX5~RX8 (V-polarization) respectively.

The two-way propagation time delay difference for each channel is:

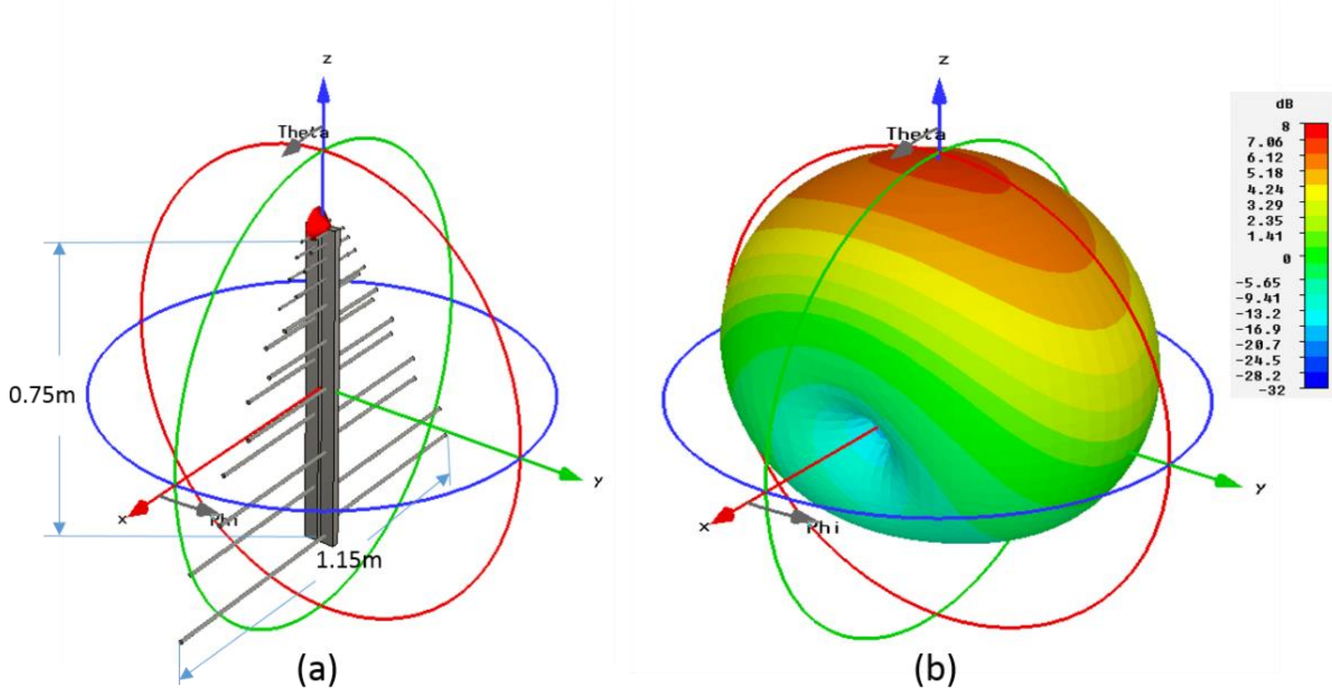

Figure S2: The geometry and radiation patterns of the 17-element log-periodic antenna. The length of the longest dipole is 1.15 m and the spacing between the shortest dipole and the longest dipole is 0.75 m. The radiation pattern was generated by using the 3D electromagnetic simulation software CST (Computer Simulation Technology) Microwave Studio.

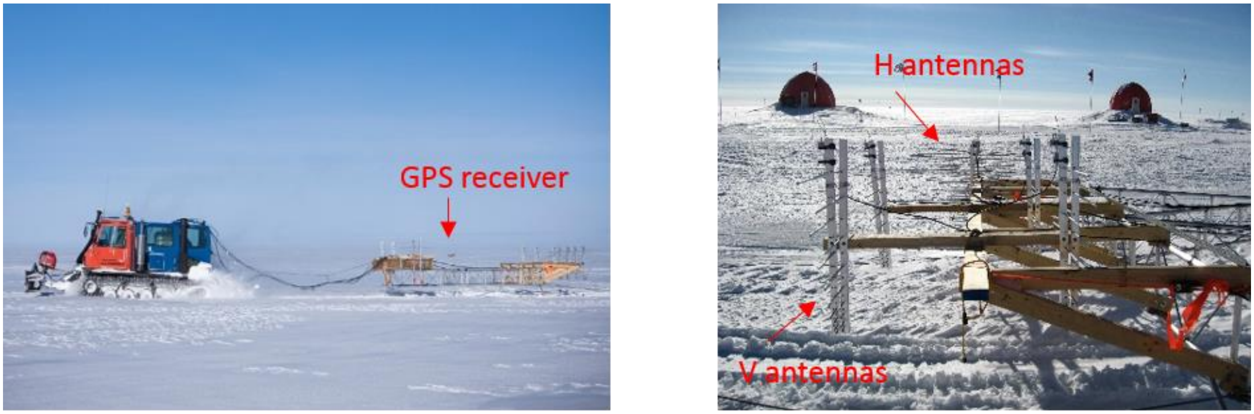

Figure S3: Multi-polarization data collection with quad-polarimetric antenna setup. Left: antennas on the sled towed by a tracked vehicle. Right: H and V receive antennas.

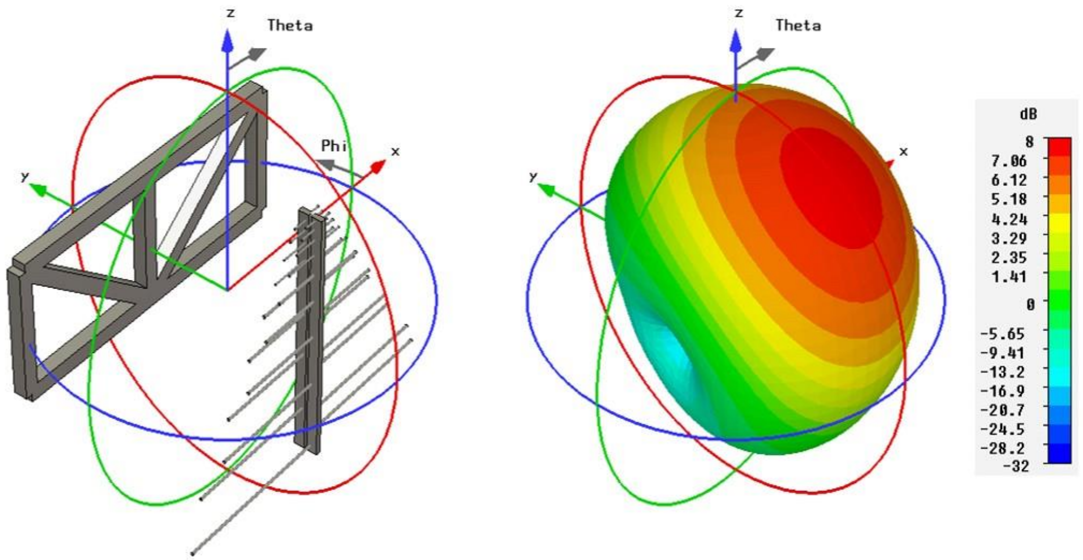

Figure S4: Truss effect on antenna radiation pattern.

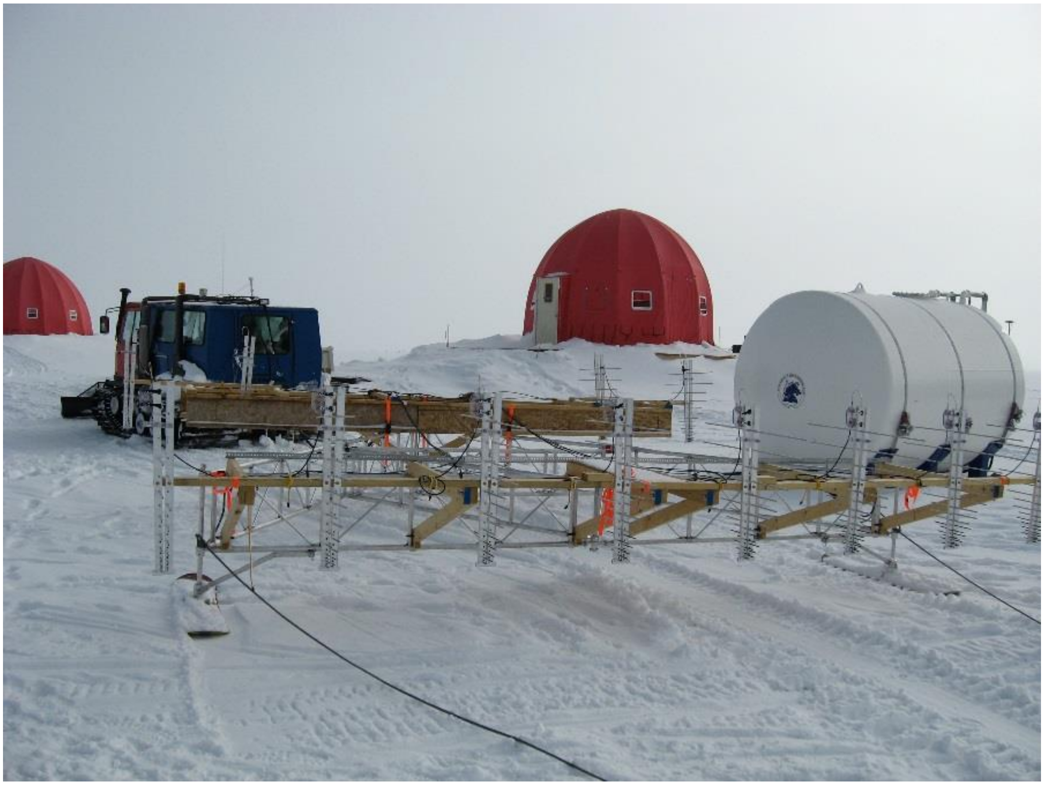

Figure S5: Truss construction and geometry

$$\nabla t_d = \sum_{l=1}^{L}\{\sum_{m=1}^{M}[t_d(l,m) - t_{d,ref}(l,m)]/M\}/L \qquad \text{(S1)}$$

where l and m are the sample and layer index respectively, $L = 3$ and $M = 1250$ are the number of layers and samples, and $t_d(l,m)$ and $t_{d,ref}(l,m)$ are the two-way propagation time delay for layer l and sample m for each channel and the reference channel, respectively. The time delay calibration needs a higher order of accuracy compared to the interval of sampling. We determined the time delay differences by oversampling the data by a factor of 100 and performing cross-correlations with the reference channel. To compensate for the time delay difference, we multiplied the data of each channel in frequency domain by $e^{j2\pi f \Delta t_d}$ where f is frequency. We then determined the amplitude and phase mismatches ΔA and Δ∅ by comparing the complex values of peak reflections from the three ice layers. Table S1 lists the channel mismatches determined through this procedure. The time delay difference between channels is less than 8.2 nanoseconds, the amplitude mismatch between channels of the same polarization is less than 3 dB, and the maximum absolute phase imbalance is less than 180°.

Table S1: Time delay ∇t_d, amplitude ΔA and phase Δ∅ mismatches between channels

	RX1, RX2, RX3, RX4	RX5, RX6, RX7, RX8
∇t_d(ns)	-2.52, 0, -0.55, 1.06	-0.79, 0, -1.24, -7.09
ΔA(dB)	2.8, 0, 1.8, 2.9	2.1, 0, 1.8, 0.4
Δ∅(°)	-162.3, 0, -91.5, -19.5	-23.9, 0, -105.6, 41.9

S4 Identification of transmit power mismatch

The power transmitted towards nadir by TX2 was about 12.7 dB less than TX1. This transmit power mismatch is shown in Fig. S6, which includes averaged power-depth profiles (incoherent integration) along the straight line perpendicular to the ice divide. These mean power-depth profiles were generated from a total of 7248 data records over a distance of 523.19m. Here we compare four pairs of transmit-receive profiles: TX1-RX4 (HH), TX1-RX5 (HV), TX2-RX4 (VH) and TX2-Rx5 (VV). Fig. S6a, S6b, S6c and S6d show the power-depth profile differences between the four different polarization combinations. The embedded zoomed-in power profiles show the power differences between the reflected specular returns from layers at depths of 1050-1350 m, including the three distinct layers at depths of 1142, 1181 and 1271 m. The peak at 2520 m is the ice-bed interface.

The transmit power mismatch between TX1 and TX2 can be determined by looking at the power differences at 1142 m. As listed in Table S2, the echoed power levels of the four polarizations P_{HH}, P_{HV}, P_{VH} and P_{VV} from this layer are -107, -115.5, -123.4 and -121.2 dB, respectively. By defining the power level differences between the four polarizations as $\Delta P_a = P_{HH} - P_{VH}$, $\Delta P_b = P_{HV} - P_{VV}$, $\Delta P_c = P_{HH} - P_{HV}$, $\Delta P_d = P_{VH} - P_{VV}$, we thus have ΔP_a, ΔP_b, ΔP_c and ΔP_d equal to $16.4, 5.7, 8.5$ and -2.2 dB respectively.

ΔP_a contains the transmit power mismatch $\Delta P_{TX} = P_{TX1} - P_{TX2}$, anisotropic reflection power difference ΔP_{ANISO}, and transmit-receive polarization mismatch ΔP_{VH} (see discussions in Section 3.3 about the polarization mismatch):

$$\Delta P_a = \Delta P_{TX} + \Delta P_{ANISO} - \Delta P_{VH} \qquad \text{(S2)}$$

ΔP_b contains the transmit power mismatch ΔP_{TX}, ΔP_{ANISO} and transmit-receive polarization mismatch ΔP_{HV}:

$$\Delta P_b = \Delta P_{TX} + \Delta P_{ANISO} + \Delta P_{HV} \qquad \text{(S3)}$$

ΔP_c contains the channel mismatch $\Delta P_{RX} = P_{RX4} - P_{RX5}$ and ΔP_{HV}:

$$\Delta P_c = \Delta P_{RX} - \Delta P_{HV} \qquad \text{(S4)}$$

ΔP_d contains ΔP_{RX} and ΔP_{VH}:

$$\Delta P_d = \Delta P_{RX} + \Delta P_{VH} \qquad \text{(S5)}$$

It is found that $\Delta P_{RX} = 1.5\, dB$ from the noise floor differences in Fig. S6c and S6d. The noise floor differences

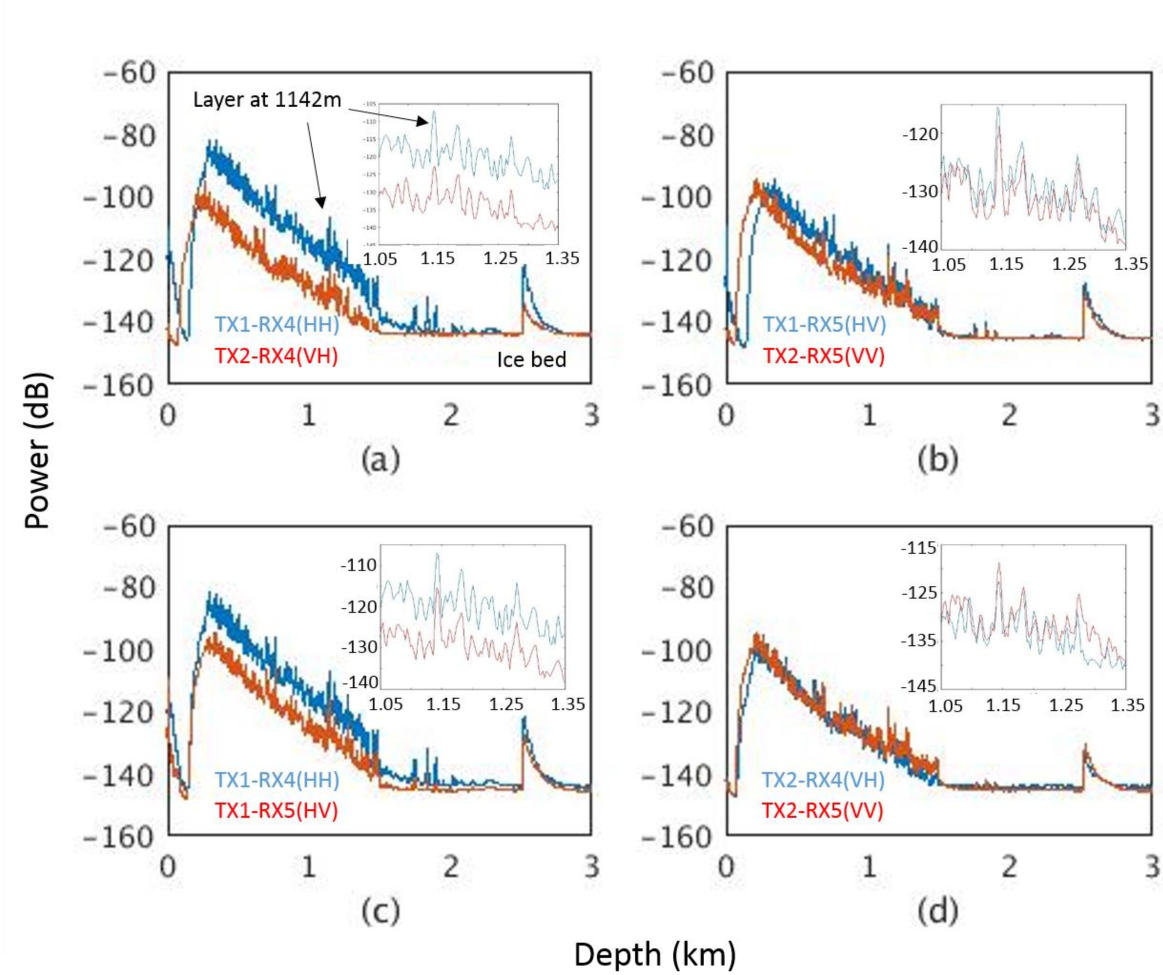

Figure S6: Averaged power-depth profiles along straight line perpendicular to the ice divide (from pt. 1 to pt. 4 in Fig. 2) for the four different Tx-Rx polarization combinations. (a) HH and VH; (b) HV and VV; (c) HH and HV; and (d) VH and VV. The insets show three specular reflection peaks from layers at depths of 1142, 1181 and 1271 m.

Table S2: Received power (in dB) of different polarizations from specular layer at depth of 1142m

	RX4 (H)	RX5 (V)	
TX1 (H)	P_{HH} = -107	P_{HV} = -115.5	$\Delta Pc = P_{HH} - P_{HV}$ = 8.5
TX2 (V)	P_{VH} = -123.4	P_{VV} = -121.2	$\Delta Pd = P_{VH} - P_{VV}$ = -2.2
	$\Delta Pa = P_{HH} - P_{VH}$ = 16.4	$\Delta Pb = P_{HV} - P_{VV}$ = 5.7	

can include other effects (such as differences in the noise figure or electromagnetic interference) but the match between the following two estimates of ΔP_{TX} indicates that these differences are small. Therefore from Eq. (S5) we have $\Delta P_{VH} = \Delta P_d - \Delta P_{RX} = -2.2 - 1.5 = -3.7\ (dB)$, and it is derived from Eq. (S2) that

$$\begin{aligned}\Delta P_{TX} &= \Delta P_a + \Delta P_{VH} - \Delta P_{ANISO} \\ &= 16.4 - 3.7 - \Delta P_{ANISO} \\ &= 12.7 - \Delta P_{ANISO}\ (dB).\end{aligned}$$

Similarly, from Eq. (S4) we have $\Delta P_{HV} = \Delta P_{RX} - \Delta P_c = 1.5 - 8.5 = -7\ (dB)$, and it is derived from Eq. (S3) that

$$\begin{aligned}\Delta P_{Tx} &= \Delta P_b - \Delta P_{HV} - \Delta P_{ANISO} \\ &= 5.7 + 7 - \Delta P_{ANISO} \\ &= 12.7 - \Delta P_{ANISO}\ (dB).\end{aligned}$$

The two ΔP_{Tx} estimates from cross comparisons match exactly. If the layer echo was from the isotropic zone (see ice anisotropy analysis in Section 3.3), then $\Delta P_{ANISO} \approx 0$ and $\Delta P_{Tx} \approx 12.7\ dB$.

We further confirmed that $\Delta P_{ANISO} \approx 0$ and $\Delta P_{Tx} \approx 12.7\ dB$ by comparing the peak power levels of HH (TX1-RX4) and VV (TX2-RX5) measurements along Circle 3, at depths in both isotropic and anisotropic zones. Along a small circle, we expect the power level of the peaks of the HH and VV measurements to be the same for two locations 90° apart on the circle because the antenna azimuth orientations of the H and V configurations are the same. However, the average power level difference between HH and VV measurements for peak pairs ~90° apart on the circle (pk1-pk3, pk2-pk4, pk5-pk10, pk6-pk11, pk7-pk12, pk8-pk9) is ~12.7 dB (see Fig. S7). The power variation patterns in Fig. S7 were obtained after the data were filtered by the 2-D moving filter described by Eq. (S6) and (S7) and discussed in supplementary section S5.

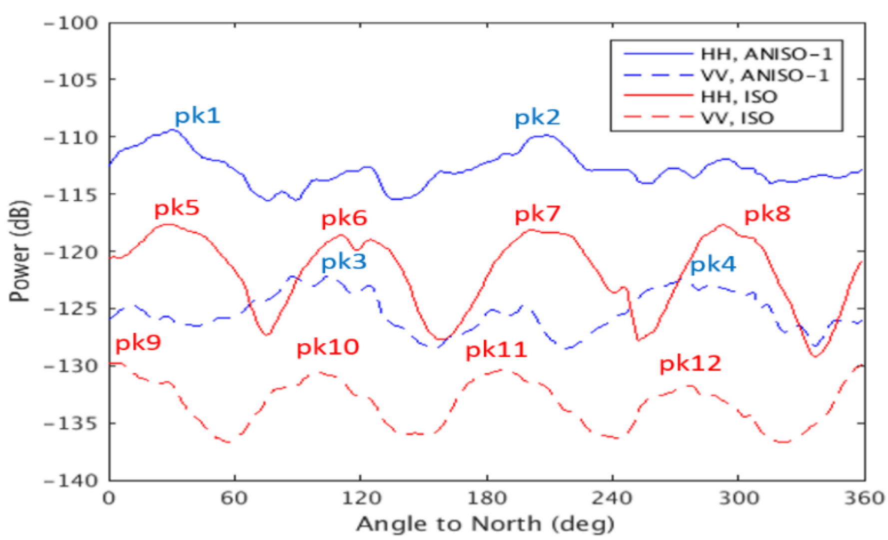

Figure S7: Power variation pattern of HH (TX1-RX4) and VV (TX2-RX5) along Circle 3. Blue lines represent the anisotropic zone ANISO-1 (see Fig. 7 a and b) at 840-m depth, red lines represent the isotropic zone at 1178-m depth, solid lines represent HH measurements and dashed lines represent VV measurements.

The 12.7-dB transmit power mismatch between TX1 and TX2 is because of the aluminium alloy truss effect and the mutual coupling between the two antennas of the transmitter in TX2, resulting in the main lobe of the radiation pattern pointing to an off-nadir direction, and other reasons currently unknown. We performed full-wave electromagnetic simulations to analyze the effect of the truss on antenna radiation characteristics, confirming the truss effect. Simulation results have shown that the radiation pattern is similar to Fig. S2b if the antenna is perpendicular to the truss, and tilts about 36° (Fig. S4) if the antenna is parallel to the truss, resulting in ~3 dB transmitted power reduction [Harish, 2008]. The real truss structure is much more complicated than the simulated one (see Fig. S5), and it may result in larger tilt and power reduction. In addition, the unconsidered mutual coupling may form nulls in the radiation pattern. According to Fig. S6a, the SNR of echoes from deep layers at depths of 1753, 1832, and 1894 m are 8.5, 11.5, and 9 dB, respectively, for TX1-RX4. However, these layers are barely visible for TX2-RX4 because of the reduced transmit power and power loss from the transmit-receive polarization mismatch. It may be worth investigating if the TX2 transmit issue could be avoided or alleviated by rotating TX2 in Fig. 1a ninety degrees instead of the arrangement in Fig. 1b.

S5 2-D Filtering of HH and HV measurements

The windowed 2-D moving average filter is described by:

$$P'_{ij} = \sum_{m=-M/2}^{M/2} \sum_{n=-N/2}^{N/2} h_{mn} P_{i+m,j+n} \tag{S6}$$

where P'_{ij} is the filtered value of power, i and j are the range bin and along-track indexes of the data matrix, $P_{i+m,j+n}$ is the value of power before this filtering, M and N are the window length and h_{mn} is the 2-D filter coefficient calculated by:

$$h_{mn} = \frac{w_{r=m+\frac{M}{2}+1} w_{s=n+\frac{N}{2}+1}}{\sum_{r=1}^{M+1} w_r \sum_{s=1}^{N+1} w_s} \tag{S7}$$

in which w_r and w_s are the window weights in range bin and along-track dimensions. This filtering removes the adverse fading effects from our analysis.

Figure S8a visualizes the filter kernel applied to convolve with the power intensity matrix. Fig. S8b compares the HH and HV power profiles at depth of 806 m before and after the filtering, illustrating that this operation can effectively smooth out the fading and extract the power variation patterns.

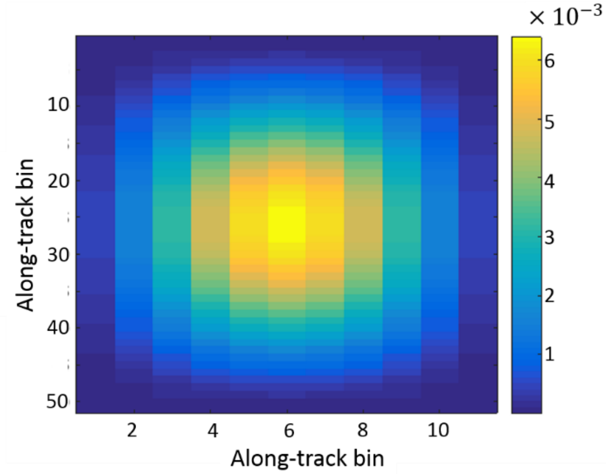

(a)

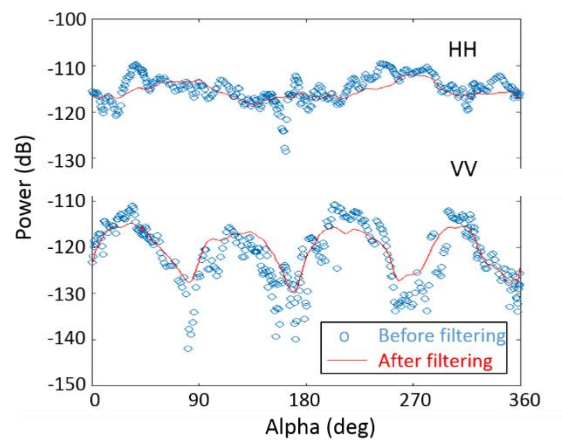

(b)

Figure S8: A 2-D moving average filter applied to data: (a) the filter kernel image; (b) comparison between data before and after filtering.

References

Harish, A. R.: Log-periodic array antenna, Technical Report, CReSIS, Feb. 25, 2008.